Complex magnetohydrodynamic low-Reynolds-number flows

Yu Xiang and Haim H. Bau*
Department of Mechanical Engineering and Applied Mechanics, University of Pennsylvania, Philadelphia, Pennsylvania 19104-6315, USA
(Received 29 January 2003; published 28 July 2003)

The interaction between electric currents and a magnetic field is used to produce body (Lorentz) forces in electrolyte solutions. By appropriate patterning of the electrodes, one can conveniently control the direction and magnitude of the electric currents and induce spatially and temporally complicated flow patterns. This capability is useful, not only for fundamental flow studies, but also for inducing fluid flow and stirring in minute devices in which the incorporation of moving components may be difficult. This paper focuses on a theoretical and experimental study of magnetohydrodynamic flows in a conduit with a rectangular cross section. The conduit is equipped with individually controlled electrodes uniformly spaced at a pitch L. The electrodes are aligned transversely to the conduit's axis. The entire device is subjected to a uniform magnetic field. The electrodes are divided into two groups A and C in such a way that there is an electrode of group C between any two electrodes of group A. We denote the various A and C electrodes with subscripts, i.e., A_i and C_i, where $i=0,\pm1,\pm2,\ldots$. When positive and negative potentials are, respectively, applied to the even and odd numbered A electrodes, opposing electric currents are induced on the right and left hand sides of each A electrode. These currents generate transverse forces that drive cellular convection in the conduit. We refer to the resulting flow pattern as A. When electrodes of group C are activated, a similar flow pattern results, albeit shifted in space. We refer to this flow pattern as C. By alternating periodically between patterns A and C, one induces Lagrangian chaos. Such chaotic advection may be beneficial for stirring fluids, particularly in microfluidic devices. Since the flow patterns A and C are shifted in space, they also provide a mechanism for Lagrangian drift that allows net migration of passive tracers along the conduit's length.

DOI: 10.1103/PhysRevE.68.016312 PACS number(s): 47.52.+j, 47.65.+a

I. INTRODUCTION

In recent years, there has been a growing interest in developing minute laboratories on a chip to facilitate chemical reactions and biological interactions. Efficient mixing and stirring of various reagents are essential to facilitate timely operation. In minute devices, stirring is a challenge since the flows are at very low Reynolds numbers, turbulence is not available to promote mixing, and it is difficult to insert moving components into these devices. Not surprisingly, a great amount of effort has been invested in devising various means for fluid stirring. One such means is based on chaotic advection or Lagrangian chaos [1]. The basic idea is to temporally and/or spatially alternate between two or more flow patterns. With an appropriate choice of such patterns, one can generate quite complicated trajectories of passive tracers. Lagrangian chaos is attractive since it does not require high Reynolds numbers. For example, various authors [1–3] have studied, theoretically and experimentally, flow through two- and three-dimensional ''twisted'' conduits. The twists (or bends) induce counter-rotating vortices that under certain conditions interact to induce chaotic advection. Stroock *et al.* [4] implemented a similar idea by machining into their flow conduits oblique grooves with different angles with respect to the flow direction. All the methods described above require a pressure source to drive the flow. In some cases, pressure sources may not be convenient to use, and it is desirable to consider alternatives.

One such alternative is the use of Lorentz forces or magnetohydrodynamics (MHD). The application of electromagnetic forces to pump, confine, and control fluids is by no means new. To date, however, magnetohydrodynamics has mostly been used to pump and control highly conducting fluids such as liquid metals and ionized gases and to study ionospheric/astrophysical plasmas [5]. The potential use of electromagnetic forces in small devices has attracted much less attention. Recently, though, Jang and Lee [6], Lemoff and Lee [7], and Zhong *et al.* [8] constructed MHD micropumps on silicon and ceramic substrates and demonstrated that these pumps are able to move liquids around in microconduits. The liquids need to be at least slightly conductive—a requirement met by many biological solutions.

Subsequently, Bau *et al.* [9–11] demonstrated the feasibility of using magnetohydrodynamic forces to control fluid flow in minute fluidic networks. The basic building block (branch) of such a network consists of a conduit with two electrodes deposited along its two opposing walls. The conduit is filled with an electrolyte solution. Many conduits are connected to form a network. The entire device is subjected to a uniform magnetic field. When a potential difference is applied across the wall electrodes, the resulting current interacts with the magnetic field to form body (Lorentz) forces that propel the fluid. By judicious application of different potential differences to different electrode pairs, one can direct the liquid to follow any desired path without the need for mechanical pumps and valves. In other words, MHD allows one to control fluid flow in a minute fluidic network in very

*Author to whom correspondence should be addressed. Electronic address: bau@seas.upenn.edu

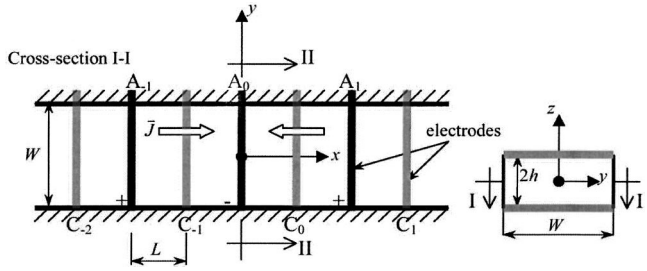

FIG. 1. Schematic top view (left) and cross section (right) depictions of the stirrer. Black gray lines correspond, respectively, to electrodes of groups *A* and *C*.

much the same way as one controls electric current flow in an electronic circuit.

Since one can readily pattern electrodes of various shapes, one can induce electric fields in different directions. The interaction of such electric fields with the magnetic field can be used to induce secondary complex flows that may be beneficial for stirring and mixing [12–14]. In this paper, we describe yet another way of inducing complex flow patterns in a conduit. The ideas articulated here can be used to construct a MHD stirrer.

The paper is organized as follows. The mathematical model is described in Sec. II. The experimental apparatus and the processing of the experimental data are detailed in Sec. III. Section IV compares the theoretical predictions with experimental observations, and Sec. V concludes. The Appendix describes refinements in the theoretical solution that facilitate accurate computation of the flow field while retaining only a few terms in the series solution.

II. MATHEMATICAL MODEL

The stirrer consists of a long, liquid-filled conduit with a rectangular cross section. Figure 1 depicts schematically the top (cross section I-I) and the side (cross section II-II) views. The conduit's width and height are, respectively, W and $2h$. The x, y, and z coordinates are, respectively, aligned along the conduit's axis, width, and height. The conduit's sidewalls are electrically insulating. Uniformly spaced electrodes are positioned transversely to the conduit's axis with a pitch L. In other words, the electrodes are placed at $x'=\pm nL$ and $z'=\pm h$, where $n=0,1,2,\ldots$. The prime denotes dimensional quantities that will later be made dimensionless. The electrodes are divided into two groups A and C in such a way that there is always an electrode of group C between any two A electrodes. The electrodes within each group are sequentially numbered as $A_{\pm n}$ and $C_{\pm n}$. For simplicity, we assume that the electrodes have zero width and height. The conduit is filled with an electrolyte solution of viscosity μ and electric conductivity σ. The conduit is positioned in a uniform magnetic field of magnitude ($\mathbf{B}=B\hat{\mathbf{e}}_z$) in the z direction.

When positive and negative potentials, respectively, are applied to even and odd numbered A electrodes, electric currents in opposite directions are induced on the left and right hand sides of the A electrodes. These currents, in turn, induce body (Lorentz) forces directed toward the conduit's sidewalls in opposite directions on the two sides of the electrodes. As a result, cellular convection is induced around the electrode with the fluid moving in the positive y direction on one side of the electrode and in the negative y direction on the other side. The cells have a width of $2L$.

According to Ohm's law for a moving conductor of conductivity σ in a magnetic field, the potential difference ($\Delta V=V_1-V_2$) induces a current of density

$$\mathbf{J}=\sigma(-\nabla V+\mathbf{u}'\times\mathbf{B}). \tag{1}$$

In the above, bold letters represent vectors; $\mathbf{u}'=\{u,v,w\}$ is the fluid's velocity; u, v, and w are, respectively, the velocity components in the x, y, and z directions; and V is the electric potential.

Since we are concerned with relatively slow flows, the term $\mathbf{u}'\times\mathbf{B}$ can be neglected. Below, we write the various equations in dimensionless form using L as the length scale. In other words, the electrodes $A_{\pm n}$ are positioned at locations $x=\pm 2n$. Furthermore, we restrict ourselves to the case $W/L\sim O(1)$ and $h/L\ll 1$. Since in our experiment $h/L=0.18$, we use the two-dimensional Hele-Shaw approximation [15]. The error induced by the Hele-Shaw approximation is estimated to be of the order of $(h/L)^2$. For further discussion of this approximation, see the appendix to Ref. [13].

The current's density in the interval between two adjacent electrodes C_{n-1} and C_n is

$$\mathbf{J}'\sim J_0[\mathrm{sgn}(x-2n)]\hat{\mathbf{e}}_x \quad (2n-1<x<2n+1), \tag{2}$$

where $J_0\sim\sigma\Delta V/2L$. Sgn(x) is positive (negative) for positive (negative) arguments, and it equals zero for a zero argument. The momentum equation has the form of Darcy's law:

$$\mathbf{u}=\frac{1}{2}[\nabla p+[\mathrm{sgn}(x-2n)]\hat{\mathbf{e}}_y] \quad (2n-1<x<2n+1). \tag{3}$$

The continuity equation is

$$\nabla\cdot\mathbf{u}=0. \tag{4}$$

Below, without loss of generality, we restrict ourselves to the interval $-1<x<1$. $\mathbf{u}=(u,v)$ is the two-dimensional velocity vector. p is the pressure. $U=J_0B_0h^2/\mu$ is the velocity scale, L/U is the time scale, and $\mu UL/h^2$ is the pressure scale. The boundary conditions include impermeable top and bottom walls,

$$\nu\left(x,\pm\frac{\hat{W}}{2}\right)=0, \tag{5}$$

and symmetry conditions at $x=\pm 1$,

$$u(\pm 1,y)=0, \tag{6}$$

where $\hat{W}=W/L$ is the aspect radio. The assumption of a zero thickness electrode results in a pressure discontinuity at $x=0$,

$$\left(\frac{\partial p}{\partial y}\right)_{x\to 0^+} - \left(\frac{\partial p}{\partial y}\right)_{x\to 0^-} = 2. \tag{7}$$

It is convenient to introduce the stream function $\Psi(x,y)$. In terms of the stream function, Eq. (3) assumes the form

$$\nabla^2\Psi = -2\sum_{k=0}^{\infty}\left\{\cos\left[\frac{(2k+1)\pi x}{2}\right]\right\} \quad (|x|\leqslant 1). \tag{8}$$

The corresponding boundary conditions are

$$\Psi\left(x,\pm\frac{\hat{W}}{2}\right)=0 \quad \text{and} \quad \Psi(\pm 1,y)=0. \tag{9}$$

Equations (8) and (9) can be readily solved, and the velocity components are

$$u=\frac{\partial\Psi}{\partial y}=\sum_{k=0}^{\infty}\frac{2}{m}\frac{\sinh(my)}{\cosh(m\hat{W}/2)}\cos[mx] \quad (|x|\leqslant 1) \tag{10}$$

and

$$\nu=-\frac{\partial\Psi}{\partial x}=-\sum_{k=0}^{\infty}\frac{2}{m}\left\{\frac{\cosh(my)}{\cosh(m\hat{W}/2)}-1\right\}\sin[mx] \quad (|x|\leqslant 1). \tag{11}$$

In the above, $m=(2k+1)\pi/2$. Later in the paper, we will compute the trajectories of passive tracers. These computations require numerous evaluations of the velocity components at different $\{x,y\}$ locations. Unfortunately, due to the singularity of the function sgn(x) at $x=0$, the series (10) and (11) converge slowly (like k^{-1}) when $|y|\to\hat{W}/2$. To overcome this shortcoming, we recast the series (10) and (11) in terms of functions that mimic the singularities of the original problem. We provide the results below and defer the derivation to the Appendix.

The series (10) and (11), rewritten in the rapidly converging form, are

$$u=-\frac{1}{2\pi}\sum_{k=0}^{\infty}(-1)^k\ln\left\{\frac{\cosh[(y+\hat{W}/2+k\hat{W})\pi]+\cos(\pi x)}{\cosh[(-y+\hat{W}/2+k\hat{W})\pi]-\cos(\pi x)}\,\frac{\cosh[(y+\hat{W}/2+k\hat{W})\pi]-\cos(\pi x)}{\cosh[(y+\hat{W}/2+k\hat{W})\pi]+\cos(\pi x)}\right\} \quad (|x|\leqslant 1) \tag{12}$$

and

$$\nu=\frac{1}{2}\mathrm{sgn}(x)-\frac{1}{\pi}\sum_{k=0}^{\infty}(-1)^k\left[\arctan\left\{\frac{\sin(\pi x)}{\sinh[(-y+\hat{W}/2+k\hat{W})\pi]}\right\}+\arctan\left\{\frac{\sin(\pi x)}{\sinh[(y+\hat{W}/2+k\hat{W})\pi]}\right\}\right] \quad (|x|\leqslant 1). \tag{13}$$

Typically, it is sufficient to retain five terms in these series to obtain a precision better than $O(10^{-5})$. For further details on the series' convergence, see the Appendix.

When the electrodes *A* are active, the flow field consists of convective cells with spatial periodicity 2. Figure 2 depicts the corresponding streamlines. The streamlines correspond to the trajectories of passive particle tracers inserted in the flow. We refer to the flow field depicted in Fig. 2 as flow pattern *A*. A similar flow field, albeit shifted distance 1 in the x direction, is observed when only electrodes *C* are active (and electrodes *A* are disconnected). We refer to the latter flow field as pattern *C*.

Next, we activate alternately electrodes *A* and *C* with the dimensionless period *T*. When the frequency of the alternations is relatively slow, one can invoke the quasistatic approximation, and the trajectories of a passive tracer particle can be computed by solving the kinematic equations

$$\dot{x}(t)=\Omega_A(t)u^{(A)}(x,y)+\Omega_C(t)u^{(C)}(x,y) \tag{14}$$

and

$$\dot{y}(t)=\Omega_A(t)\nu^{(A)}(x,y)+\Omega_C(t)\nu^{(C)}(x,y) \tag{15}$$

with the initial conditions $x(0)=x_0$, $y(0)=y_0$. The subscripts *A* and *C* refer, respectively, to patterns *A* and *C*. The time-dependent functions $\Omega_A(t)$ and $\Omega_C(t)$ define the stirring protocol. One can explore various types of time modulation [various functions $\Omega(t)$]. For brevity, we select the simple on-off protocol

$$\Omega_A(t)=\begin{cases}1, & nT<t<\left(n+\frac{1}{2}\right)T,\\ 0, & \left(n+\frac{1}{2}\right)T<t<(n+1)T,\end{cases}$$

$$\Omega_C(t)=\begin{cases}0, & nT<t<\left(n+\frac{1}{2}\right)T,\\ 1, & \left(n+\frac{1}{2}\right)T<t<(n+1)T.\end{cases} \tag{16}$$

The resulting flow field is periodic in time with periodicity *T*. Aref and Balachandar [1] investigated the effects of various protocols on the kinematics of the flow between two rotating, eccentric cylinders and determined that an on-off protocol

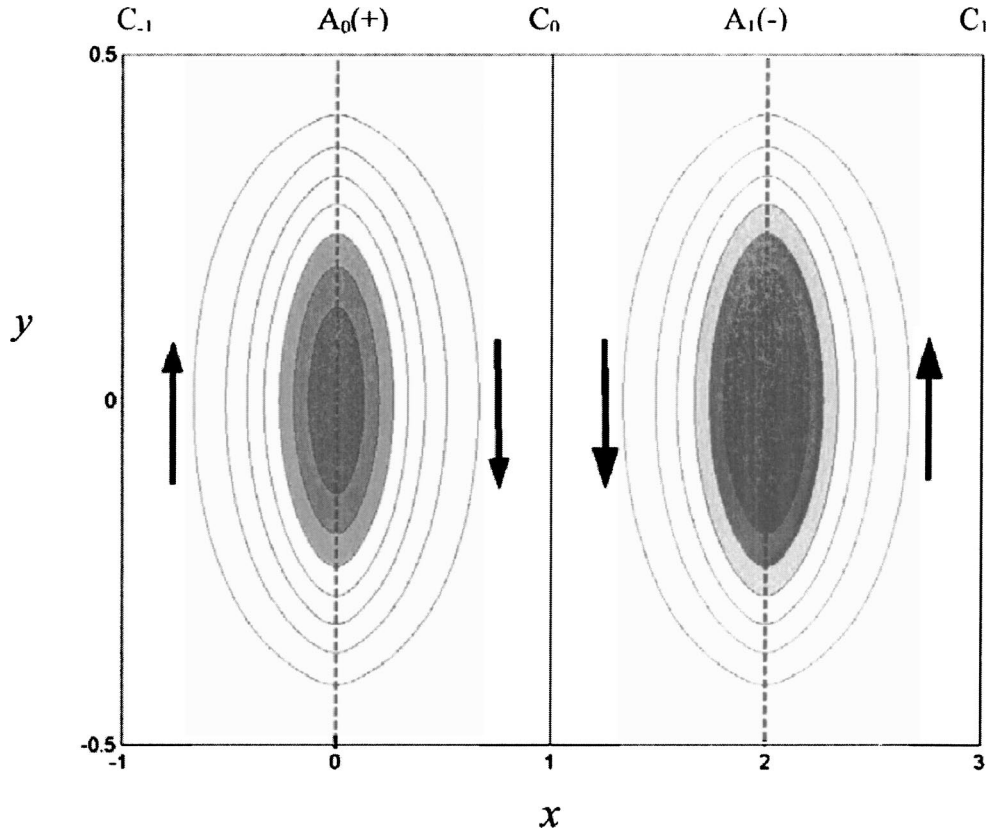

FIG. 2. The streamlines when electrodes of type *A* are continuously active. The dashed lines depict the positions of the active electrodes. The arrows indicate the flow direction.

gives qualitatively indistinguishable results compared to those obtained with smoother protocols. Finally, we note that the more interesting flow phenomena occur when T is relatively large and when the quasistatic approximation is likely to be valid.

Although physically unrealistic, it is instructive to study the flow field in the limit of $T \to 0$ (high switching frequency). In this limit, Eqs. (14) and (15) form a Hamiltonian system, and they are integrable. Figure 3 depicts the superposed flow field $A+C$. The figure illustrates the existence of saddle (hyperbolic) points at $\{x,y\}=\{(4k+1)/2,0\}$ $(k \in Z)$ (see the magnified image on the right). Saddle (hyperbolic-fixed) points are desirable since when they are perturbed chaotic advection and efficient stirring result [16].

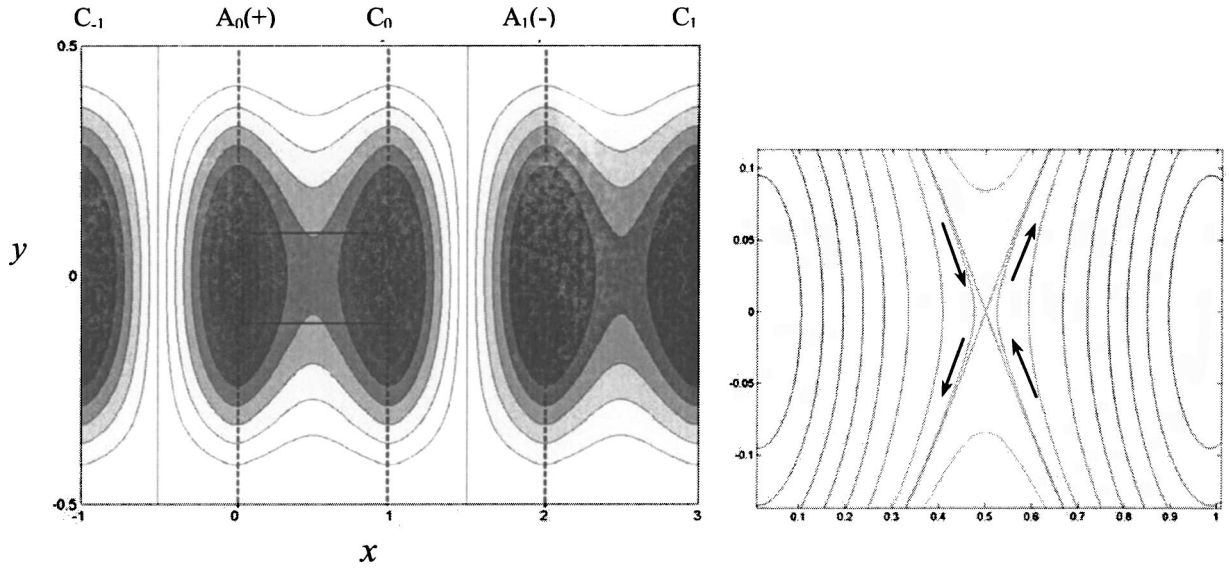

FIG. 3. The superposed streamlines of flow patterns *A* and *C*. The dashed lines depict the positions of the electrodes. The inset on the right depicts a magnified view of the saddle point region.

When $T>0$, Eqs. (14) and (15) are no longer integrable, and we must resort to numerical techniques. To this end, we use the fourth order accurate Runge-Kutta solver (ODE45) in MATLAB. The predicted flow patterns when $T>0$ are reported in Sec. IV.

III. EXPERIMENTAL APPARATUS AND PROCEDURE

To verify the theoretical predictions, we carried out flow visualization experiments. The apparatus consists of a conduit of length 750 mm, width $W=5.0$ mm, and height $2h=2.8$ mm fabricated with Proteus Homopolymer (Poly Hi Solidur). To facilitate easy flow visualization, we did not cap the conduit in the experiments. The electrodes were formed with 0.5 mm diameter copper wires stretched along the conduit's bottom. The electrodes were uniformly spaced with a pitch of $L=7.5$ mm. The conduit was filled with $0.1M$ sodium chloride (NaCl) solution.

The electrodes were divided into two groups. Each group was connected through a computer-controlled relay actuator (Advantech PCL735) to a power supply (Hewlett-Packard 6032A). The device was positioned on top of a neodymium (NdFeB, Polymag Inc.) permanent magnet that provided a nearly uniform magnetic field of intensity $B\sim 0.4$ T. The magnetic field's intensity was measured with a gaussmeter.

The electric potentials applied to the electrode groups were about 1.5 V and the total electric current in the flow cell was 1.15 ± 0.25 mA. At this potential level, there was no significant bubble generation. The current was measured with a Digital Multimeter (Hewlett-Packard 3458A).

In some of the experiments, we visualized the flow field by introducing a drop of dye (Fluorescent Liquid Dye, Cole-Parmer Instrument Company, with an estimated diffusion coefficient of 2.5×10^{-9} m^2/s) at various locations inside the channel and tracking its evolution as a function of time. In other experiments, we traced a line of dye along the conduit's midwidth and tracked its deformation as a function of time. The spread and progression of the dye were monitored with a digital camera (Nikon Cooplix 995).

To obtain some estimate of the experimental time constant, we compared the predicted and measured velocities at $\{x,y\}=\{0.5,0\}$. The theory predicts that the dimensionless velocity (v) in the y direction is about 0.25. The corresponding value measured in the experiments was 1 mm/s. We conclude therefore that the velocity scale in the experiments is $U\sim 4$ mm/s and that the corresponding time scale is $L/U\sim 1.8$ s. Comparisons between predicted and observed dye traces indicated, however, that a better qualitative agreement between theory and experiment was obtained when a somewhat smaller time constant of 1 s was used.

The color images obtained from the experiments were transferred to MATLAB's image processing toolbox. The number of pixels that were contained in the image depended on the size and quality of the image. Typically a pixel represented a square area of 0.1×0.1 mm^2. Before the introduction of the dye, we took an image of the experimental setup to obtain the ''background.'' Subsequently, the background was subtracted from all the images. The process is illustrated in Fig. 4. Figures 4(a) and 4(b) are, respectively, the gray scale versions of the photographs of the original image at the start of the experiment and the same image after the subtraction of the background.

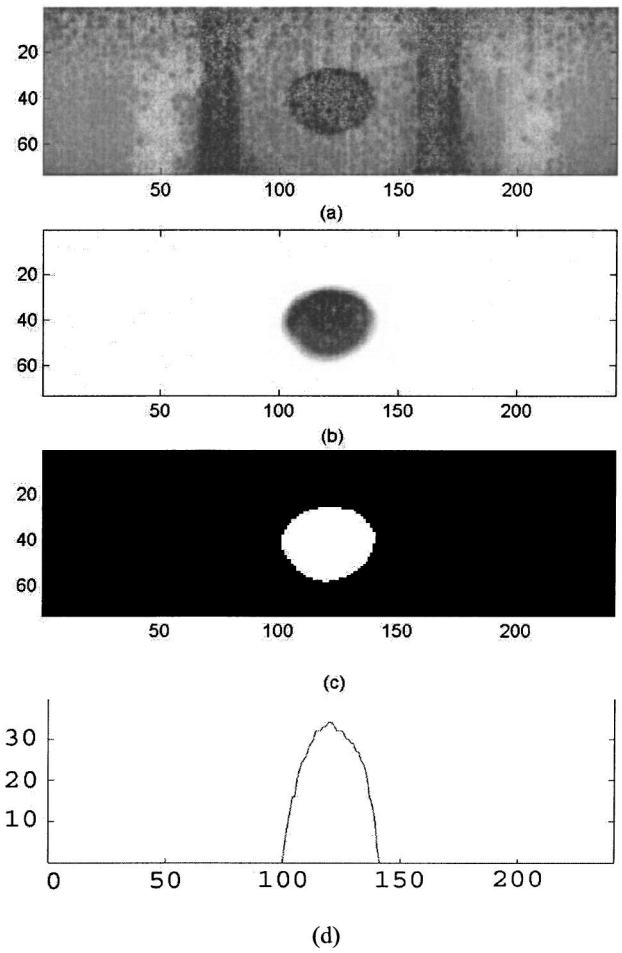

FIG. 4. Image processing steps to obtain the area covered with dye as a function of time: (a) raw image; (b) image after background subtraction; (c) image pixels assigned value of 0 (black) in the absence of dye and 1 (white) in the presence of dye; and (d) the sum of the pixels along the y coordinate as a function of x.

To monitor the area occupied by the dye, we constructed a filter. Briefly, the computer assigned to each pixel three numbers corresponding to the red, green, and blue color intensities. We found it convenient to work with the green color. The green intensity of pixel (i,j) was denoted $g_{i,j}$. The contrast level of the image was intensified using the contrast enhancement filter within MATLAB [17]. In brief, each pixel's value was recalculated as a weighted average of itself and its nearest neighbors. Subsequently, the pixel values $(g_{i,j})$ were normalized to a scale ranging between 0 and 1. Next, the average intensity was calculated and denoted as $\overline{g}$. A threshold value $g_0=\overline{g}+\mu$ was defined, where μ was assigned the value of 0.15. Pixels with values $g_{i,j}\geqslant\overline{g}$ and $g_{i,j}<\overline{g}$ were assigned, respectively, values of 1 and 0.

Figure 4(c) depicts the processed image in which the pixels were assigned values of 1 (white) and 0 (black). Finally, we counted the total number of the 1-valued pixels to obtain the areas covered by dye at various times. Alternatively, one can find the sum of the 1-valued pixels at any x location to

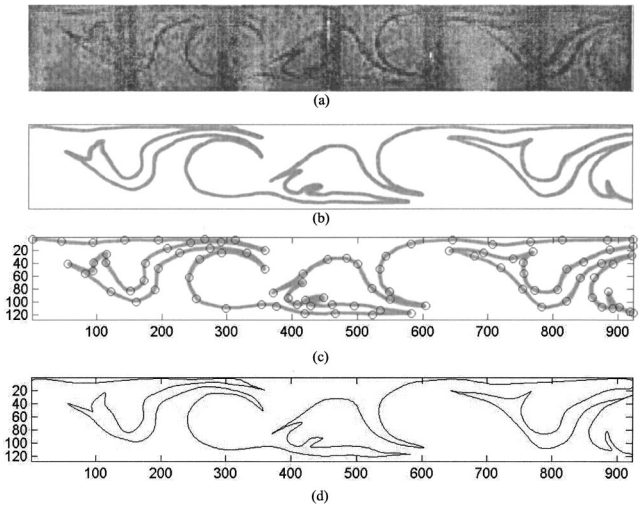

FIG. 5. Image processing steps to obtain the length of an initially straight trace of dye as a function of time. $T=t=4$. (a) Raw image; (b) image after manual retouch and background subtraction; (c) nodes chosen for spline approximation; (d) an approximated piecewise polynomial curve determined with the spline function in MATLAB.

obtain the dye-occupied pixels as a function of x. Figure 4(d) is an example of the sum of the pixels' values along the y direction as a function of x.

The reduction in the dye's intensity is a result of the molecular diffusion process. In the absence of diffusion, the area occupied by the dye would have been conserved. Nevertheless, the rate of the spread of the dye provides a measure of the stirring efficiency since, as the length of the interface between the dyed and clear fluid increases, molecular diffusion becomes more effective. Hence, indirectly, the rate of the spread of the dye provides an indirect measure of the rate of elongation of the interface between the dye blob and the clear fluid.

Our attempts to measure the edge length of the blob of dye as a function of time were frustrated by the complex topology of this interface. As an alternative, we tracked the length of an initially straight trace of dye as a function of time. The processing steps of the experimental data are depicted in Fig. 5. Figure 5(a) is the photograph of an initially straight trace of dye inserted along the device's midheight. The figure was retouched manually to improve the contrast between the dye and the background in the electrodes' vicinity. Subsequently, the background was subtracted [Fig. 5(b)]. We started with MATLAB's edge recognition routine to identify the pixels associated with the line's boundaries. When we compared the values obtained with this method with known lengths of calibration curves, we observed a relatively large error (about 20%). As an alternative, we used MATLAB's spline function to approximate the curve locally with piecewise continuous (cubic) polynomials. To this end, we specified interpolating nodes (pixels) on the line trace [shown as circles in Fig. 5(c)]. The precision of this approximation increases as the number of nodes increases. An example of a fitting spline curve is depicted in Fig. 5(d). The length of the line was estimated by integrating the piecewise continuous interpolating functions. The lengths of calibration curves obtained with the spline technique were in excellent agreement with known values.

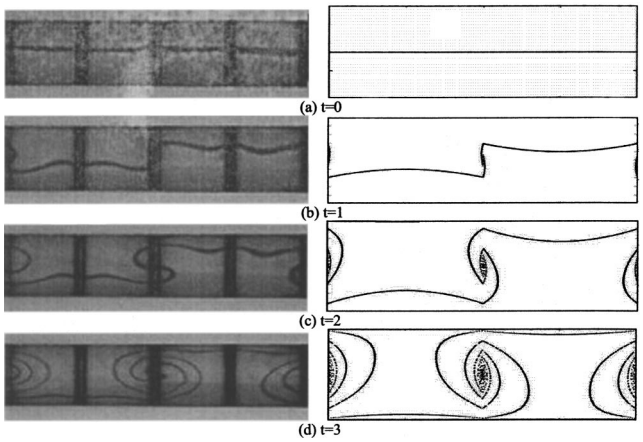

FIG. 6. Deformation of an initially straight line of dye placed at the channel's midheight. Electrodes A are continuously active. The left and right columns correspond, respectively, to experimental observations and theoretical predictions at various times $t=0$ s (a), 1 s (b), 2 s (c), and 3 s (d).

IV. RESULTS AND DISCUSSION

We carried out numerical simulations and flow visualization experiments for various periods T. We started by comparing the experimental results and the theoretical predictions when only one set of electrodes is active (i.e., electrodes A). Both in the experiment and theory, we tracked the evolution of an initially straight line of ''dye'' inserted along the conduit's midwidth. Figure 6 depicts the dye trace at various times. The left and right columns correspond, respectively, to the experimental observations and the theoretical predictions. Figures 6(a), 6(b), 6(c), and 6(d) correspond, respectively, to times $t=0$, 1, 2, and 3. The traces are consistent with a set of counter-rotating convective cells of width $2L$ centered about electrodes A_n. The experiments and theory are in good qualitative agreement.

When $T=2$ s, Fig. 7 depicts the experimental observations (left) and theoretical predictions (right) of the evolution of a drop of dye at times $t=0$ (a), T (b), $2T$ (c), $3T$ (d), $4T$ (e), $5T$ (f), $6T$ (g), $7T$ (h), $8T$ (i), and $12T$ (j). To facilitate the comparison with theory, we processed the experimental image at time $t=0$ to obtain the coordinates of the drop. This provided us with the initial conditions for the numerical integration. The theoretical images were obtained by integrating the trajectories of 1500 passive tracer ''particles.'' The experimental observations and theoretical predictions are in good qualitative agreement: witness the stretching and folding that are characteristic of chaotic advection. The chaotic island is, however, confined to a small region around the superposed trajectory of flow patterns A and C that passes through the hyperbolic fixed point. It is instructive to compare Fig. 7(j) with Fig. 3. The presence of the saddle, hyperbolic point is clearly visible. When T is small, the passive tracer trajectories approximately track the streamlines asso-

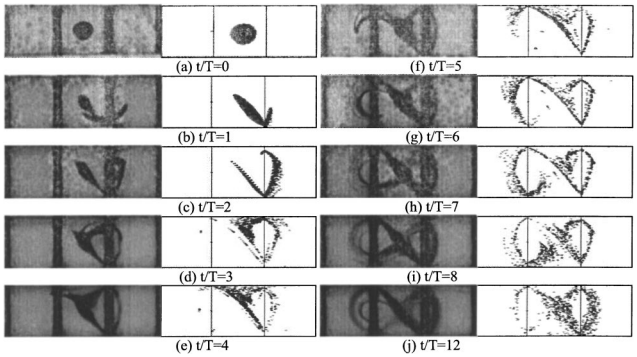

FIG. 7. The spread of a blob of dye as a function of time $t/T=0$ (a), 1 (b), 2 (c), 3 (d), 4 (e), 5 (f), 6 (g), 7 (h), and 8 (i). The left and right columns at each time correspond, respectively, to experimental data and theoretical predictions. The alternation period $T=2$ s.

ciated with the superposed flows.

As T increases so does the size of the chaotic region. Figure 8 depicts the experimental observations and the theoretical predictions for the spread of a drop of dye when $T=5$ s. As in Fig. 7, the image at the beginning of the experiment was processed to obtain the locations of the pixels associated with the area occupied by the dye at $t=0$. These pixels then provided the initial conditions for the numerical simulations. In the numerical simulations, we integrated the trajectories of about 3000 points that the image processing algorithm identified as having a pixel value of 1 at time $t=0$. Figure 8 depicts the evolution of the drop of dye at times $t=0.2T$ (a), $0.4T$ (b), $0.6T$ (c), $0.8T$ (d), T(e), $1.2T$ (f), $2T$ (g), and $3T$ (h). The theoretical predictions are in good qualitative agreement with experimental observations.

Figure 8 illustrates yet another phenomenon—that of drift. Since flow patterns A and C are shifted by half a spatial period, there is a mechanism for net migration of tracer particles along the conduit's length. Even though there is no net through flow, there is net migration of particles. We refer to this migration as a Lagrangian drift. Although this phenomenon is somewhat reminiscent of dispersion, the mechanism of the Lagrangian drift is different. It would be interesting to devise an ''effective diffusivity'' for the Lagrangian drift. Unfortunately, we have not found a convenient way for doing so, short of massive numerical simulations.

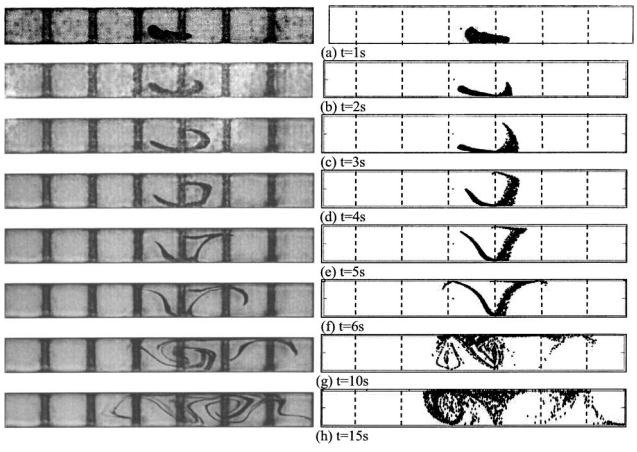

FIG. 8. The spread of a blob of dye as a function of time $t/T=0.2$ (a), 0.4 (b), 0.6 (c), 0.8 (d), 1 (e), 1.2 (f), 2 (g), and 3 (h). The left and right columns correspond, respectively, to experimental data and theoretical predictions. The alternation period $T=5$ s.

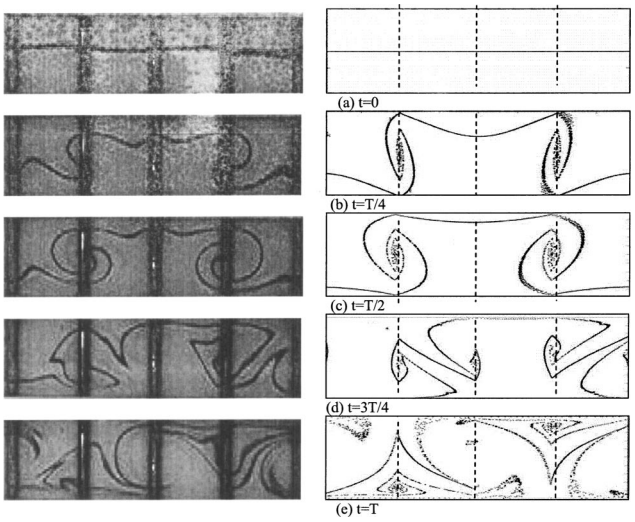

FIG. 9. Deformation of an initially straight line of dye placed at the channel's midheight. The left and right columns correspond, respectively, to experimental observations and theoretical predictions at various times $t/T=0$ (a), 1/4 (b), 1/2 (c), and 1 (d). $T=4$ s.

It is also instructive to follow the evolution of an initially straight line of dye under chaotic flow conditions. When $T=4$ s, Fig. 9 depicts the experimental observations (left) and theoretical predictions (right) for an initially straight line of dye at times $t=0$ (a), $T/4$ (b), $T/2$ (c), $3T/4$ (d), and T (e). In the numerical simulation, we integrated the trajectories of 4000 uniformly spaced points. The images depict the stretching and folding process associated with chaotic advection. The figure illustrates good qualitative agreement between experiment and theory.

An important issue from the engineering point of view is the quantification of the stirring efficiency. We use the dye's rate of spread as the measure of the stirrer's performance. Using the MATLAB image processing toolbox, we processed the photographs of the experiments at various times. Employing a filter (see Sec. III), we identified whether various pixels were occupied by dye or not. We normalized the dyed area $A(t)$ at time t with the initial area occupied by the dye drop $A(0)$ at time 0 to obtain the dimensionless area $\hat{A}(t)=A(t)/A(0)$. Figure 10 depicts the dimensionless area $\hat{A}(t)$ as a function of t when $T=2$, 5, and 10. The symbols and solid lines correspond, respectively, to experimental data and best fit curves (see below). Clearly, as T increases so does the rate of increase of $\hat{A}(t)$. To obtain a single figure of merit, we used regression to fit curves of the form $\exp(\lambda t)$ to the experimental data. In the above, λ represents the growth rate of the area occupied by the dye. The growth rate λ is depicted as a function of the period T in Fig. 11. In the range of our experimental parameters, λ increases as T increases according to the correlation $\lambda=e^{T/T_0}-1$, where $T_0=37.3$. λ

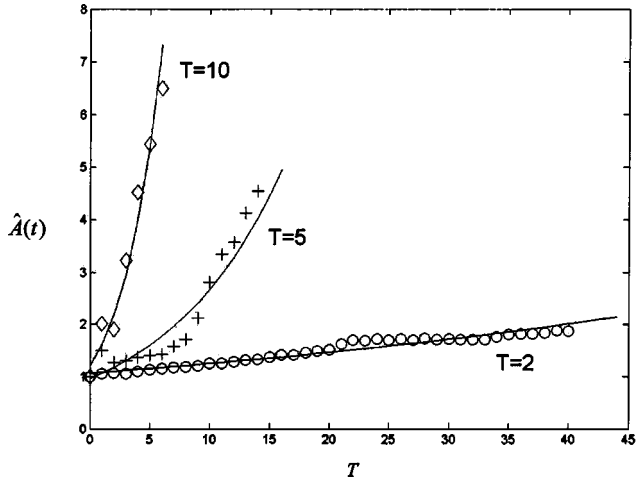

FIG. 10. The dimensionless area $\hat{A}(t)$ as a function of t when $T=2$, 5, and 10. The symbols and solid lines correspond, respectively, to experimental data and the best fit curve.

plays a similar role to that of the Lyapunov exponent, and it can be used as a measure of the intensity of the chaotic advection.

Similarly, one can determine the amount of time that it takes for the area occupied by the dye to double. We denote the ''doubling'' time as τ. Figure 12 depicts τ as a function of the period T. In the range of our experimental parameters, τ decreases as T increases. This behavior is described well by a correlation of the form $\tau \sim \ln T^n + \tau_0$, where $n \sim -9$ and $\tau_0 \sim 23$. We attempted to calculate the variance of the color intensity as a function of time [18–20]. However, the results of these calculations were not particularly illuminating.

As we noted in Sec. III, in the absence of diffusion, the area occupied by the dye would be conserved [$\hat{A}(t) = \text{const}$]. The continuous stretching and folding of the interface between the dyed liquid and the clear water enhances the molecular diffusion process. Thus the rate of increase of the dyed area is a measure of the combined effects of stirring and molecular diffusion.

The elongation rate of the boundary between the dyed blob and the clear fluid is likely to provide a better measure of the stirring effectiveness. We were not able to track this

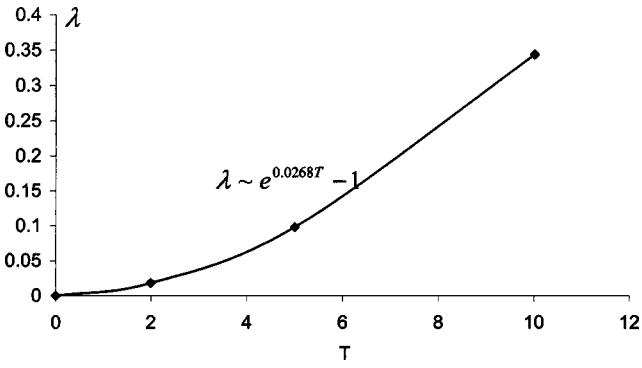

FIG. 11. The growth rate λ as a function of the period T. The symbols and solid lines correspond, respectively, to the experimental data and the best fit curve.

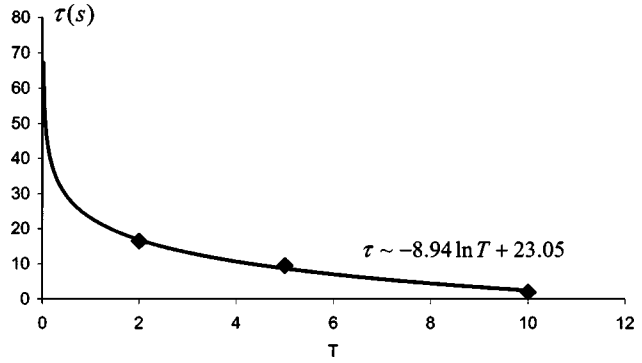

FIG. 12. The doubling time τ as a function of the period T. The symbols and solid lines correspond, respectively, to the experimental data and the best fit curve.

interface. As an alternative, we tracked the elongation rate of an initially straight stretch of dye inserted at the device's midheight (Figs. 6 and 9). Figure 13 depicts the relative length $\hat{L}(t) = L(t)/L(0)$ as a function of time for flow patterns A (squares, no alternations) and A-C (diamonds, alternation period $T=4$). When the electrode potentials were not alternated, the line elongated nearly linearly according to the correlation $\hat{L}(t) \sim 1 + 0.4t$. In the presence of chaotic advection (flow pattern C, $T=4$), the elongation rate was exponential and correlated well with $\hat{L}(t) \sim \exp(0.33t)$. The positive growth rate of 0.33 is consistent with chaotic advection.

We conclude our discussion with a few comments on the suitability of MHD stirring for microdevices. The MHD force is a volumetric one. Hence, as the size of the device decreases, the magnitude of the velocity decreases rapidly. There are, however, a few mitigating factors. As the characteristic length decreases, the current intensity increases. The characteristic velocity in terms of the electrode potential difference (V) is $U = \sigma V B_0 h^2/\mu L$, where σ is the electrolyte's electric conductivity. Typically, the threshold potential for the hydrolysis of water dictates the maximum electrode potential. Hence, we assume that this potential difference will remain the same regardless of device size. Within a period T,

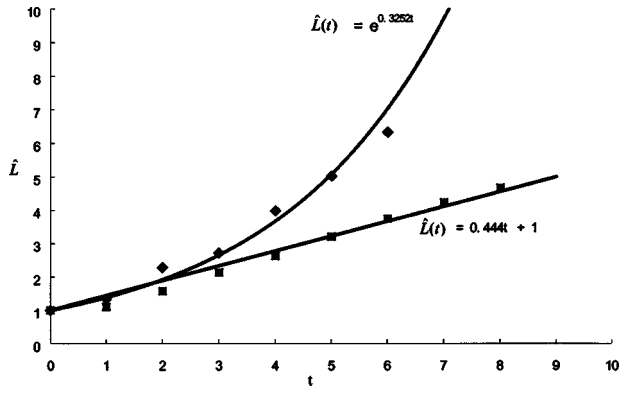

FIG. 13. The relative length $\hat{L}(t)$ of an initially straight trace of dye as a function of time. The symbols and solid lines correspond, respectively, to the experimental data and the best fit curve. The squares and diamonds correspond, respectively, to dc actuation and periodic potential alternation. $T=4$.

a passive tracer particle travels a relative distance $UT/L = (\sigma V B_0 T/\mu)(h/L)^2$. If we accept the argument that different size stirrers perform similarly when the passive tracer particle travels similar relative distances within a period T, we may conclude that as long as T and V remain the same and h and L are scaled down in like proportions, the stirrer's performance will be size invariant.

V. CONCLUSIONS

This paper demonstrates that magnetohydrodynamics provides a convenient way of inducing complicated flow patterns that may be of interest for both fundamental research and practical applications. The flow patterns are controlled by the electrodes' pattern and the potentials applied to the various electrodes. Photolithography provides a great amount of flexibility for patterning electrodes. In our particular example, we demonstrated that by positioning the electrodes transverse to the conduit's axis and engaging only one group of electrodes, one can generate cellular convection. By alternately engaging two staggered groups of electrodes, one can induce chaotic advection. As the period of alternations increases, so does the intensity of the chaotic motion. The chaotic motion facilitates effective stirring. A method was used to evaluate the stirrer's efficiency through image processing. In the range of parameters examined in this paper, the stirrer's ''efficiency'' increased as the period of alternations increased. Stirrers operating according to the concepts described here may be useful for microfluidic systems since they do not require any moving components and can be fabricated readily with standard planar microfabrication technology. The theoretical predictions were in good agreement with experimental observations, suggesting that the modeling can be used as an effective tool for the design and optimization of the stirrer. Interestingly, the chaotic flow also provides a mechanism for the net transport of passive particle tracers along the length of the conduit. We refer to this phenomenon as Lagrangian drift. The Lagrangian drift becomes more pronounced as the period of the alternations increases. The drift is somewhat reminiscent of dispersion, but it is caused by a different physical mechanism. The phenomenon can probably be quantified through the use of an effective diffusion coefficient. We defer the derivation of such a diffusion coefficient to future work.

APPENDIX: ACCELERATED RATE OF CONVERGENCE

Equations (10) and (11) of Sec. IV provide expressions for the velocity components in series form. Unfortunately, when y approaches $W/2$, the series converge slowly (like k^{-1}), and it may not be practical to use these solutions to compute the passive tracers' trajectories. The slow convergence of series (10) and (11) results from the series attempting to approximate a singular function. This gives rise to the Gibbs phenomenon and slow convergence. Happily, one can recast the series in a form that allows rapid convergence. Briefly, we expand the hyperbolic functions in the series into geometric series to obtain double series. Subsequently, we change the order of summation. This allows us to sum the new inner series in a closed form. The new closed form functions mimic the singularities of the original expression. Thus, the resulting series converges very rapidly. The various steps of the derivation are straightforward, and they are outlined below. We start with the series solution for u:

$$
\begin{aligned}
u &= \sum_{n=0}^{\infty} \frac{2}{m} \frac{\sinh(my)}{\cosh(m\hat{W}/2)} \cos[mx] \\
&= -\sum_{n=0}^{\infty} \frac{2}{m} \frac{e^{m(y-\hat{W}/2)}(1-e^{-2my})}{(1+e^{-m\hat{W}})} \cos[mx] \\
&= -\sum_{n=0}^{\infty} \left\{ \frac{2}{m} e^{m(y-\hat{W}/2)}(1-e^{-2my}) \cos[mx] \sum_{k=0}^{\infty} (-1)^k e^{-mk\hat{W}} \right\} \\
&= -\sum_{k=0}^{\infty} (-1)^k \left\{ \sum_{n=0}^{\infty} \frac{2}{m} e^{m(y-\hat{W}/2-k\hat{W})}(1-e^{-2my}) \cos[mx] \right\} \\
&= -\sum_{k=0}^{\infty} (-1)^k \left\{ \sum_{n=0}^{\infty} \frac{2}{m} e^{m(y-\hat{W}/2-k\hat{W})} \cos[mx] \right\} + \sum_{k=0}^{\infty} (-1)^k \left\{ \sum_{n=0}^{\infty} \frac{2}{m} e^{m(-y-\hat{W}/2-k\hat{W})} \cos[mx] \right\}. \qquad \text{(A1)}
\end{aligned}
$$

Applying the identity [21]

$$
\sum_{n=0}^{\infty} \frac{1}{[1+2n]} \exp[-(2n+1)t] \cos[(2n+1)x] = \frac{1}{4} \ln\left[\frac{\cosh t + \cos x}{\cosh t - \cos x} \right], \qquad \text{(A2)}
$$

we have

$$u=-\frac{1}{2\pi}\sum_{k=0}^{\infty}(-1)^k\ln\left\{\frac{\cosh[(-y+\hat{W}/2+k\hat{W})\pi]+\cos(\pi x)}{\cosh[(-y+\hat{W}/2+k\hat{W})\pi]-\cos(\pi x)}\,\frac{\cosh[(y+\hat{W}/2+k\hat{W})\pi]-\cos(\pi x)}{\cosh[(y+\hat{W}/2+k\hat{W})\pi]+\cos(\pi x)}\right\}. \tag{A3}$$

Similarly,

$$\begin{aligned}
\nu&=-\sum_{n=0}^{\infty}\frac{2}{m}\left[\frac{\cosh(my)}{\cosh(m\hat{W}/2)}-1\right]\sin[mx]=-\sum_{n=0}^{\infty}\frac{2}{m}\frac{e^{my}+e^{-my}}{e^{m\hat{W}/2}+e^{-m\hat{W}/2}}\sin[mx]+\sum_{n=0}^{\infty}\frac{2}{m}\sin[mx]\\
&=-\sum_{n=0}^{\infty}\frac{2}{m}\frac{e^{m(y-\hat{W}/2)}(1+e^{-2my})}{(1+e^{-m\hat{W}})}\sin[mx]+\sum_{n=0}^{\infty}\frac{2}{m}\sin[mx]\\
&=-\sum_{n=0}^{\infty}\left\{\frac{2}{m}e^{m(y-\hat{W}/2)}(1+e^{-2my})\sin[mx]\sum_{k=0}^{\infty}(-1)^k e^{-mk\hat{W}}\right\}+\sum_{n=0}^{\infty}\frac{2}{m}\sin[mx]\\
&=-\sum_{k=0}^{\infty}(-1)^k\left\{\sum_{n=0}^{\infty}\frac{2}{m}e^{m(y-\hat{W}/2-k\hat{W})}(1+e^{-2my})\sin[mx]\right\}+\sum_{n=0}^{\infty}\frac{2}{m}\sin[mx]\\
&=-\sum_{k=0}^{\infty}(-1)^k\left\{\sum_{n=0}^{\infty}\frac{2}{m}e^{m(y-\hat{W}/2-k\hat{W})}\sin[mx]\right\}-\sum_{k=0}^{\infty}(-1)^k\left\{\sum_{n=0}^{\infty}\frac{2}{m}e^{m(-y-\hat{W}/2-k\hat{W})}\sin[mx]\right\}+\sum_{n=0}^{\infty}\frac{2}{m}\sin[mx].
\end{aligned} \tag{A4}$$

Next, we apply the identities [21]

$$\sum_{n=0}^{\infty}\frac{1}{[1+2n]}\exp[-(2n+1)t]\sin[(2n+1)x]=\frac{1}{2}\arctan\left[\frac{\sin x}{\sinh t}\right] \tag{A5}$$

and

$$\sum_{n=0}^{\infty}\frac{1}{[1+2n]}\sin[(2n+1)t]=\frac{\pi}{4}\mathrm{sgn}(t),\quad -\pi<t<\pi, \tag{A6}$$

to obtain

$$\begin{aligned}
\nu=&\frac{1}{2}\mathrm{sgn}(x)-\frac{1}{\pi}\sum_{k=0}^{\infty}(-1)^k\\
&\times\left[\arctan\left\{\frac{\sin(\pi x)}{\sinh[(-y+\hat{W}/2+k\hat{W})\pi]}\right\}\right.\\
&\left.+\arctan\left\{\frac{\sin(\pi x)}{\sinh[(y+\hat{W}/2+k\hat{W})\pi]}\right\}\right].
\end{aligned} \tag{A7}$$

In the above, $-1<x<1$. Given the periodicity in x, the formula can be readily extended for $|x|>1$.

The series (A3) and (A7) converge rapidly. For example, when $\hat{W}=2/3$, the first six terms in the series for $v(0.5,0.5)$ are 2.573×10^{-1}, 9.89×10^{-2}, -1.200×10^{-2}, 1.510×10^{-3}, 1.823×10^{-4}, and 2.245×10^{-5}. Figure 14 depicts the vertical velocity $v(x,0)$ as a function of x when $\hat{W}=2/3$, using Eq. (11) with five terms (dashed line), Eq. (11) with 100 terms (solid line), and the accelerated series (A7) with five terms (circles). Witness that Eq. (11) exhibits the Gibbs phenomenon (oscillatory, nonphysical behavior) while the accelerated series behaves smoothly.

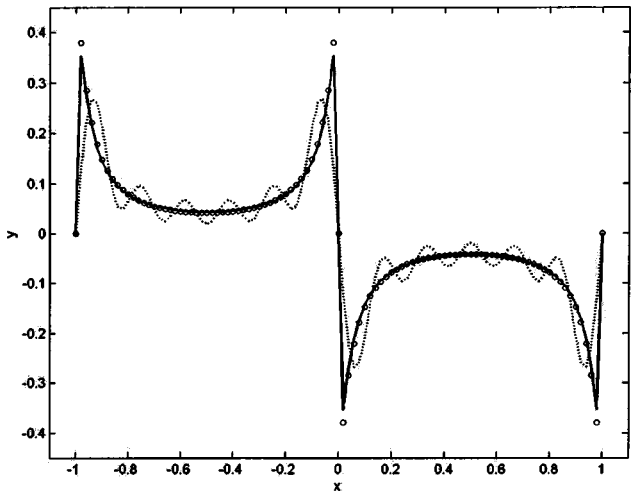

FIG. 14. The velocity $v(x,9/20)$ as a function of x calculated with series (11) with five terms (dashed line), series (11) with 100 terms (solid line), and Eq. (A7) with five terms (circles).

[1] H. Aref and S. Balachandar, Phys. Fluids **29**, 3515 (1986).
[2] R. H. Liu *et al.*, J. Microelectromech. Syst. **9**, 190 (2000).
[3] M. Yi and H. H. Bau, in *Proceedings, ASME-IMECE 2000, MEMS 2, Orlando, FL, 2000*, edited by A. P. Lee, J. Simon, F. K. Foster, and R. S. Keynton (ASME, New York, 2000), p. 489; also Int. J. Heat Fluid Flow (to be published); DOI: 10.1016/S0142-727X(03)00026-2.
[4] A. D. Stroock *et al.*, Science **295**, 647 (2002).
[5] P. A. Davidson, *An Introduction to Magnetohydrodynamics* (Cambridge University Press, Cambridge, England, 2001).
[6] J. S. Jang and S. S. Lee, Sens. Actuators A **80**, 84 (2000).
[7] A. V. Lemoff and A. P. Lee, Sens. Actuators B **63**, 178 (2000).
[8] J. Zhong, M. Yi, and H. H. Bau, Sens. Actuators A **96**, 59 (2002).
[9] H. H. Bau, in *ASME-IMECE 2001, MEMS 23884, Symposium Proceedings, New York, 2001*, edited by K. Breuer, C. Meinhart, A. Beskok, J. Santiago, E. Cummings, C. C. Wong, F. Forster, R. Zengerle, and D. Liepmann (ASME, New York, 2001).
[10] H. H. Bau, J. Zhong, and M. Yi, Sens. Actuators B **79**, 205 (2001).
[11] H. H. Bau, J. Zhu, S. Qian, and Y. Xiang, Sens. Actuators B **88**, 205 (2003).
[12] H. H. Bau, J. Zhong, and M. Yi, Sens. Actuators B **79**, 207 (2001).
[13] M. Yi, S. Qian, and H. H. Bau, J. Fluid Mech. **468**, 153 (2002).
[14] S. Qian, J. Zhu, and H. H. Bau, Phys. Fluids **14**, 3584 (2002).
[15] G. K. Batchelor, *An Introduction to Fluid Dynamics* (Cambridge University Press, Cambridge, 1967).
[16] H. Aref, J. Fluid Mech. **143**, 1 (1984).
[17] Computer code MATLAB, Release 13, The Math Works, Inc., Boston, 2002, image processing toolbox.
[18] P. Danckwerts, Appl. Sci. Res., Sect. A **3**, 279 (1952).
[19] J. M. Ottino and D. V. Khakhar, Annu. Rev. Fluid Mech. **32**, 55 (2000).
[20] P. G. M. Kruijt *et al.*, AIChE J. **47**, 1005 (2001).
[21] F. Oberhettinger, *Fourier Expansions* (Academic Press, New York, 1973).